

Nanostructured Back Reflectors for Efficient Colloidal Quantum-Dot Infrared Optoelectronics

Se-Woong Baek, Pau Molet, Min-Jae Choi, Margherita Biondi, Olivier Ouellette, James Fan, Sjoerd Hoogland, F. Pelayo García de Arquer, Agustín Mihi,* and Edward H. Sargent*

Colloidal quantum dots (CQDs) can be used to extend the response of solar cells, enabling the utilization of solar power that lies to the red of the bandgap of c-Si and perovskites. To achieve largely complete absorption of infrared (IR) photons in CQD solids requires thicknesses on the micrometer range; however, this exceeds the typical diffusion lengths (≈ 300 nm) of photoexcited charges in these materials. Nanostructured metal back electrodes that grant the cell efficient IR light trapping in thin active layers with no deterioration of the electrical properties are demonstrated. Specifically, a new hole-transport layer (HTL) is developed and directly nanostructured. Firstly, a material set to replace conventional rigid HTLs in CQD devices is developed with a moldable HTL that combines the mechanical and chemical requisites for nanoimprint lithography with the optoelectronic properties necessary to retain efficient charge extraction through an optically thick layer. The new HTL is nanostructured in a 2D lattice and conformally coated with MoO_3/Ag . The photonic structure in the back electrode provides a record photoelectric conversion efficiency of 86%, beyond the Si bandgap, and a 22% higher IR power conversion efficiency compared to the best previous reports.

Colloidal quantum dots (CQD) combine bandgap tunability with low manufacturing cost facilitated by solution processing.^[1] Lead chalcogenide CQDs provide absorption and emission tuned into the infrared (IR)—a regime of interest in sensing,^[2] machine vision, autonomous driving, and solar energy harvesting.^[3]

IR CQDs extend the response of photovoltaic technologies further into the IR region of the solar spectrum, serving as

the back cell in a tandem structure with perovskite ($E_g = 1.58\text{--}1.68$ eV)/CQD or Si ($E_g = 1.1$ eV)/CQD.^[4,5] The solar spectrum contains up to 15 mA cm^{-2} of potential short-circuit current beyond 1100 nm (Figure 1a), and this corresponds to as many as 7 additional absolute power conversion efficiency (PCE) points additive atop those provided by c-Si.^[5]


The absorption coefficient of lead chalcogenides in the IR range is $\approx 10^4\text{ cm}^{-1}$ at the excitonic peak. Thus $\approx 1\text{ }\mu\text{m}$ of active layer material is needed, in a conventional planar device, to absorb IR photons from 1100 to 1800 nm. Unfortunately, the carrier diffusion lengths in solid CQD are limited to a few hundred nanometers, and this absorption–extraction trade-off has so far limited the efficiency of IR photon harvesting to 3.9% (>perovskite) and a 1.1% (>c-Si).^[6]

Light management strategies have sought to increase CQD absorption in the IR range to overcome the absorption–extraction compromise. These include the use of multilayers as cavities,^[7] plasmonic nanoparticles,^[8,9] and grating structures.^[10,11] In particular, nanostructuring of the metal back mirror has been advanced as a means to enhance absorption by increasing the optical path within the active layer of the material.^[10,12] To date, though, the realization of structured back mirrors has come at a cost to backside charge collection and has been accompanied by increased surface recombination.

Here, we report nanostructured photonic back electrodes that achieve enhanced IR light trapping via the direct nanostructuring of a new organic hole transport layer. We replace conventional, rigid 1,2-ethanedithiol-exchanged CQD hole transport layers (HTLs) in CQD devices with a moldable HTL consisting of a PBDTTT-E-T, a copolymer of benzo[1,2-b:4,5-b']dithio-phene (BDT) and thieno[3,4-b]thiophene (TT). The new HTL combines the mechanical properties required for nanoimprint lithography with the hole mobility and the band alignment needed to achieve efficient charge extraction. We imprint this HTL using a 2D periodic pattern that is then conformally coated with MoO_3/Ag . The resulting photonic electrodes increase IR absorption and simultaneously provide efficient hole extraction. As a result, we achieve a record

Dr. S.-W. Baek, Dr. M.-J. Choi, M. Biondi, O. Ouellette, J. Fan, Dr. S. Hoogland, Dr. F. P. García de Arquer, Prof. E. H. Sargent
Department of Electrical and Computer Engineering
University of Toronto
10 King's College Road, Toronto, Ontario M5S 3G4, Canada
E-mail: ted.sargent@utoronto.ca

P. Molet, Dr. A. Mihi
Institut de Ciència de Materials de Barcelona (ICMAB-CSIC)
Campus de la UAB 08193 Bellaterra, Catalonia, Spain
E-mail: amih@icmab.es

 The ORCID identification number(s) for the author(s) of this article can be found under <https://doi.org/10.1002/adma.201901745>.

DOI: 10.1002/adma.201901745

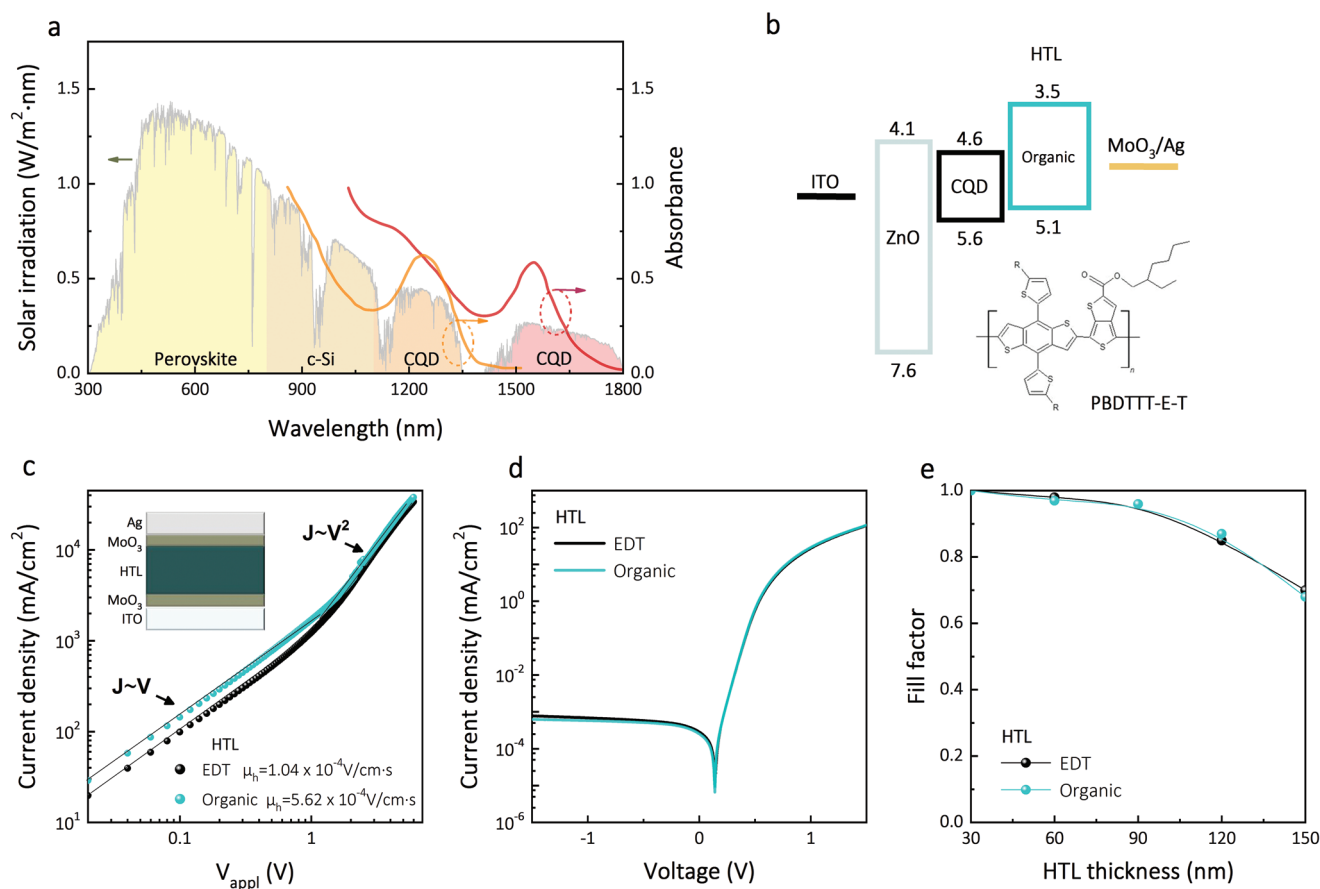


Figure 1. a) AM 1.5 Solar irradiation (left) versus range of operation of widely used solar technologies and absorbance curves of infrared CQD with different crystal size (right). b) Energy level diagram of full CQD device structure and chemical structure of organic polymer used as an HTL. c) Hole mobility of EDT (black) and organic (blue) HTL, respectively. Black lines denote linear fits curves to linear and quadratic regimes. d) J - V curves under dark conditions of CQD-EDT (black) and organic (blue) HTL. e) FF dependence of IR CQD devices with the thickness of the HTL layer for CQD-EDT-deposited (blue) and organic-deposited (black) HTL.

photoelectric conversion efficiency of 86% at 1220 nm and an infrared PCE (the solar PCE experienced by AM1.5 filtered solar light longer than 1100 nm) of 6.5%—a 22% increase compared to best previous reports—resulting in the potential addition of 1.34% extra PCE points on top of Si photovoltaics (PVs).

For semiconducting materials such as organics^[13] and perovskites,^[14] direct poly(dimethylsiloxane) (PDMS) imprinting of the active layer before metal evaporation has previously been used to form back photonic electrode structures.^[13] In the case of CQD solar cells, a structured active layer has been formed by spin-casting CQDs onto a corrugated mold-on-substrate; and then transferring the now-back-side-structured active layer onto a new ETL stack; however, this approach did not deliver a significant net advance in PCE because it was accompanied by increased surface recombination leading to V_{oc} and FF losses.^[10,11] Alternative approaches such as molding the HTL have so far been precluded by the rigidity of the 1,2-ethanedithiol (EDT)-treated CQD HTL layer (Figure S1, Supporting Information).

We sought to replace conventional EDT HTLs with new materials that were compatible with soft nanoimprint lithography. The optimal HTL should be easily deformed by gently

pressing with the PDMS mold with minimal chemical interaction. From an optoelectronic standpoint, the HTL would require appropriate band alignment with the CQD active layer (Figure 1b), and sufficient charge carrier mobility for holes to enable the incorporation of imprinted features relevant to the spectral regime of interest compatible with efficient hole extraction.

We began by exploring poly(3,4-ethylenedioxythiophene)-poly(styrenesulfonate) (PEDOT:PSS), a well-known organic material with high conductivity. We found that the high surface tension of water (72 dynes cm⁻¹ at 25 °C) prevented the homogeneous deposition over the CQD solid film (Figure S2a,b, Supporting Information), resulting in the formation of not uniform inhomogeneous films unfavorable for patterning.

We then turned our attention to soft conjugated polymers, which possess elastic properties compatible with molding during assembly (they exhibit a lower surface tension of 33 dynes cm⁻¹ at 25 °C when dissolved in chlorobenzene), and tunable highest occupied molecular orbital (HOMO) levels to facilitate hole-extraction from the CQD active layer. With these considerations in mind, we screened various conjugated polymers seeking to select the best moldable HTL for

CQD devices (Figure S2c, Supporting Information). Among them, we selected PBDTTT-E-T, a copolymer of BDT and TT (Figure 1b),^[15] which exhibited the highest yield of extraction of photogenerated carriers, adequate charge transport properties, and surface tension during self-assembly (Figure S2d, Supporting Information). PBDTTT-E-T has been used as the active layer in organic solar cells in combination with n-type phenyl-C₆₁-butyric acid methyl ester (PCBM) and nonfullerene acceptors;^[15] here we focus instead on their use as the HTL in CQD optoelectronic devices.

We compared the performance of the candidate organic HTL with that of conventional EDT-treated CQD (CQD-EDT) layers. We used the space charge limited current (SCLC) method to estimate mobility.^[16] The overall structure of SCLC devices was indium tin oxide (ITO)/MoO₃/HTL (EDT-CQD or the organic layer)/MoO₃/Ag (Figure 1c). The layer of MoO₃ was deposited on ITO as an electron-blocking layer in this electrode. The measured hole mobilities for the CQD-EDT and PBDTTT-E-T were 1×10^{-4} and 6×10^{-4} V cm⁻¹ s⁻¹, respectively, indicating that the organic layer provides a hole mobility advantage relative to the conventional approach. The resultant mobilities agree well with those seen in previous reports.^[17]

To test further the performance of this new organic HTL, we fabricated full CQD devices including this layer in an ITO/ZnO/IR CQD layer/HTL/MoO₃/Ag configuration and characterized current–voltage characteristics under dark conditions. Both HTLs exhibit comparable transport properties at similar thicknesses (≈ 65 nm) (Figure 1d). We tracked the FF of both devices as a function of HTL thickness, as thicker HTLs would allow the incorporation of photonic structures with deeper corrugation and stronger scattering efficiency (Figure 1e). The CQD device that used the PBDTTT-E-T HTL maintained 83–85% of the initial FF until a HTL thickness of 100 nm under 1 sun illumination.

We then sought to design photonic nanostructures that enhance IR absorption based on this material choice using finite-difference time-domain (FDTD) modelling. In our simulations (Figure 2), we studied the influence of the geometry of the photonic structure, but restricted the thicknesses of the active and electron/hole transport layers to those compatible with efficient optoelectronic operation (e.g., maximum HTL layer thickness was restricted to 150 nm). We focused our attention on photonic architectures formed by square arrays of cylinders, which have shown to produce broad light absorption enhancement in thin film systems.^[18] The absorption enhancement was calculated with respect to a planar device with the same active layer thickness and 80 nm HTL thickness—the optimal planar device with the highest PCE. We began by exploring the lattice periodicity (L) and the depth of the cylinders in the HTL (h) to tune the enhancement toward the wavelengths of interest and maximize its intensity (Figure 2a,b). The depth of the cylinder enables the system with photonic modes (Figure 2a) whose position can be tuned with the lattice parameter (Figure 2b). Theoretically, features with depths beyond 100 nm could provide stronger scattering from the photonic structure, but this would be at the expense of diminished electrical transport, as well as increasing the risk of shunting (Figure 1e).

In Figure 2b, we can differentiate the photonic modes sustained by the plasmonic crystal in the solar cell. In this diagram, we encounter modes whose frequency remains invariant to changes in the lattice parameter such as the resonance observed at 867 nm (i), (Figure 2b). The absorption enhancement peaks whose frequency depends on the lattice parameter are highlighted in Figure 2b as ii, iii. At these wavelengths, the backscattered light of the photonic electrode couples to the photonic resonances specifically provided by the periodicity of the array, being trapped within the active layer of the material. Further insight can be gained by studying the spatial distribution of the power absorbed at the resonances i, ii, iii from Figure 2b for the planar and the photonic electrode configuration. The spatial absorption profile in the flat architectures (Figure 2e,g,i) presents a standing wave absorption profile while patterned devices (Figure 2f,h,j) show higher overall absorptions and distinct electromagnetic field profiles. The resonance appearing at 867 nm (i) is located around the cylinder structure following its dipolar mode (Figure 2f), whereas resonances located at 1155 and 1281 nm correspond to lattice modes caused by the diffraction of the 2D photonic crystal into the CQD film (Figure 2h,j).

From our simulations, the photonic architecture that maximizes IR absorption near the 1100–1400 nm interest region (near the excitonic peak) consists of a square array of 110 nm deep holes in the organic HTL with a periodicity of $L = 500$ nm over a 520 nm thick IR CQD dots layer (Figure 2d). By doing so, we achieved absorption peaks of +30% at 1155 and 1281 nm and even achieved a 10% extra absorption at the maximum of the excitonic peak at 1220 nm. The integrated absorption enhancement in the >1100 nm regime was 12% (better observed in Figure 4). The influence of other device parameters such as the organic and CQD layer thicknesses led to optimum values around 20 and 520 nm, respectively (Figure S3, Supporting Information).

The preferred array pattern was implemented into CQD devices with the aid of soft nanoimprinting lithography (NIL),^[19] an approach that has enabled the nanostructuring of a wide range of materials.^[9,20] NIL produces high-resolution patterns over large areas and is scalable and compatible with roll-to-roll techniques. We used a prepatterned PDMS stamp to mold the HTL. First we spin-cast the organic HTL onto the flat CQD film on a glass/ITO/ZnO substrate. Immediately following spin coating, and while the polymer was still wet, we gently pressed the PDMS stamp against the sample for 2 min. After we removed the stamp, the organic layer showed consistent iridescence across the region of indentation. Atomic force microscopy (AFM) revealed the resulting 2D hole squared array structure to have 110 nm depth from the 130 nm total thickness of the HTL (Figure 3b). The nanostructured layer produced via NIL retains a residual layer of imprinted material (in our case 20 nm) that prevents completely perforating the imprinted film: this is important to prevent shunts. Scanning electron microscopy (SEM) cross-sectional images reveal the morphology for the photonic HTL structure (Figure 3c).

To complete the devices, we thermally evaporated 20 nm of MoO₃ and 400 nm of Ag on top of the patterned HTL (Figure S4, Supporting Information). The thick silver layer provided a smooth and uniform coating of the organic template,

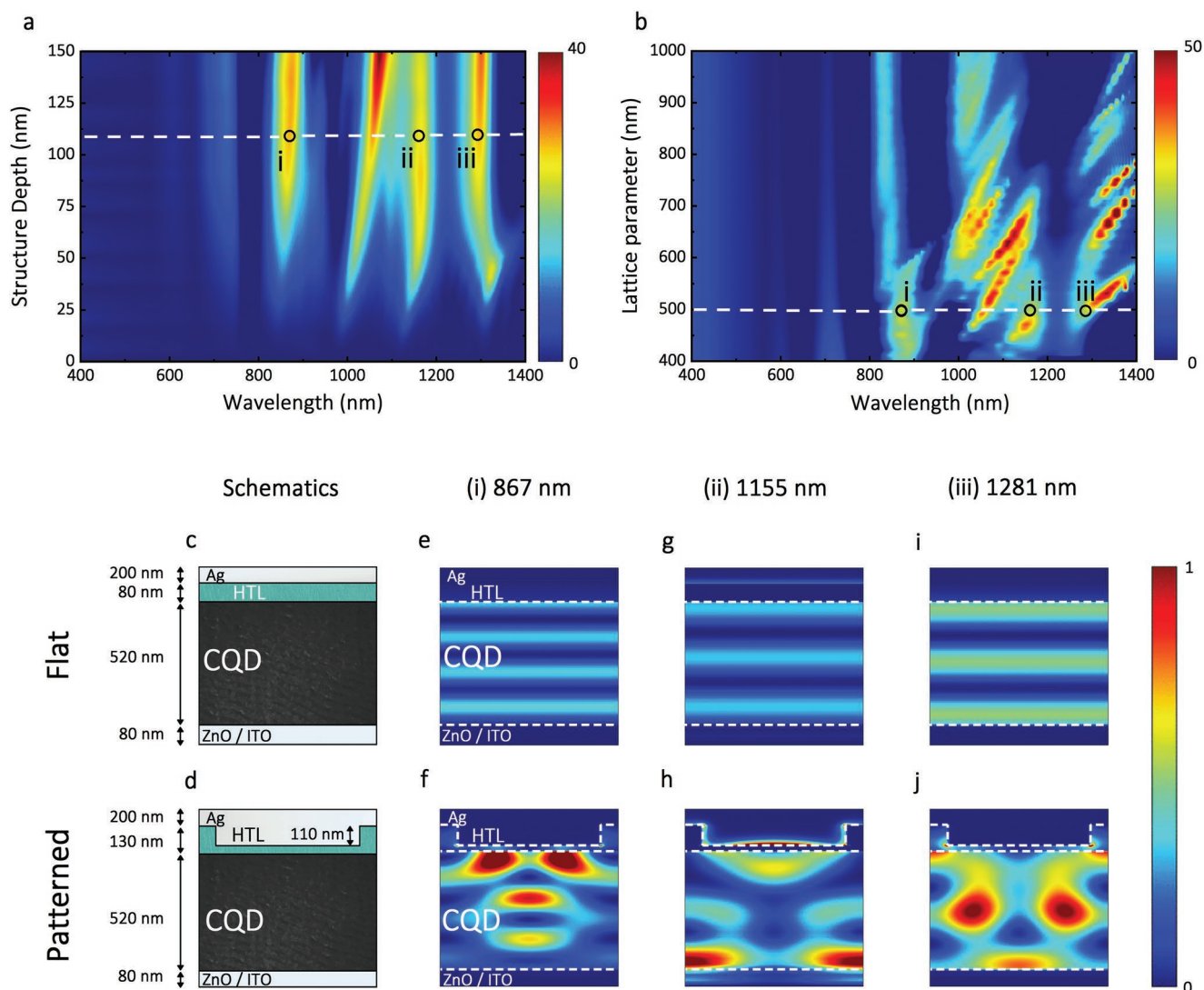


Figure 2. a) Calculated absorption enhancement for patterned 520 nm thick IR CQD active layers at normal incidence as a function of wavelength and structure depth and b) structure lattice parameter L . Schematic cross-sections of c) flat and d) patterned devices and cross-sectional absorption maps at enhancement wavelength peaks: e, f) 867 nm, g, h) 1155 nm, and i, j) 1281 nm for flat and imprinted devices, respectively.

retaining thereby the structures (Figure 3d) designed with the aid of FDTD. The final CQD devices (Figure 2) retained the desired diffraction of light as viewed from the electrode side (Figure 3e).

The external quantum efficiency (EQE) of IR CQD solar cells exhibits broad spectral responses from 350 to 1400 nm and strong excitonic peaks near 1220 nm (Figure 4a). The photonic electrodes lead to a 14% J_{sc} enhancement, raising the original J_{sc} of 32 mA cm⁻² of flat devices to 36 mA cm⁻² in patterned ones. The EQE improved across the entire 350–1400 nm spectral range and was most significant in the IR range 1000–1400 nm. With a maximum EQE of 86% at 1220 nm, these photonic electrode devices set a new record EQE relative to prior IR CQD photoelectric devices, including both solar cells and photodetectors.^[21]

To ascertain the origin of the EQE enhancement, we compared the measured absorption and measured EQE of each

device, both flat and patterned devices (Figure S5, Supporting Information). Their spectral features correlated closely between $A(\lambda)$ and $EQE(\lambda)$. Correspondingly, the estimated internal quantum efficiency (IQE) was comparable, and varied minimally with λ , for flat and patterned devices (Figure 4a).

We then measured the J - V characteristics for both flat and patterned IR CQD devices under AM 1.5 illumination with a silicon cut-off filter (allowing illumination for $\lambda > 1100$ nm) (Figure 4b,c). The PCE of the devices with the photonic electrode is statistically higher than that of flat devices. In IR region, the flat device generated 4.4 mA cm⁻² and the patterned device 5.6 mA cm⁻², achieving a J_{sc} 27% enhancement with comparable V_{oc} and FF (Table 1).^[6,22]

In summary, we designed and fabricated CQD solar cells with photonic back electrodes that improve absorption within the CQD solid especially in the IR range. To fabricate the photonic structure within the HTL, we replaced the

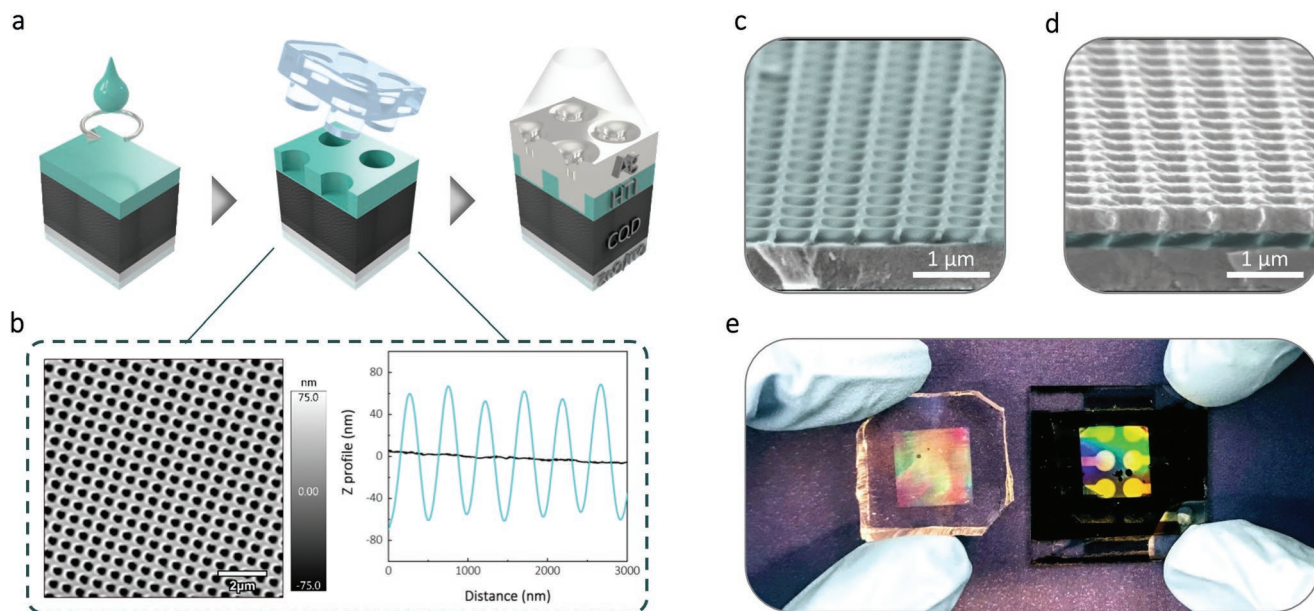


Figure 3. a) Schematics of the PDMS imprinting process in CQD devices. b) Surface images and line profile of organic layer scanned by AFM after imprinting. Scale bar: 2 μm . c) SEM images of organic hole transporting template after imprinting (left) and d) final metal structure deposited onto the organic template. e) Photograph of the prepatterned PDMS mold (left) and the final IR CQD device after nanoimprinting (right).

conventional rigid EDT-treated CQD HTL with a soft, patternable conjugated copolymer with high hole mobility and a band alignment conducive to the egress of holes from the CQD active layer into the contact. Soft nanoimprinting added to the

HTL fabrication procedure enabled the enhanced EQE and PCE in the spectral regime beyond silicon's absorption. This work indicates a strategy to seamlessly integrate light trapping in solution-processed IR optoelectronics.

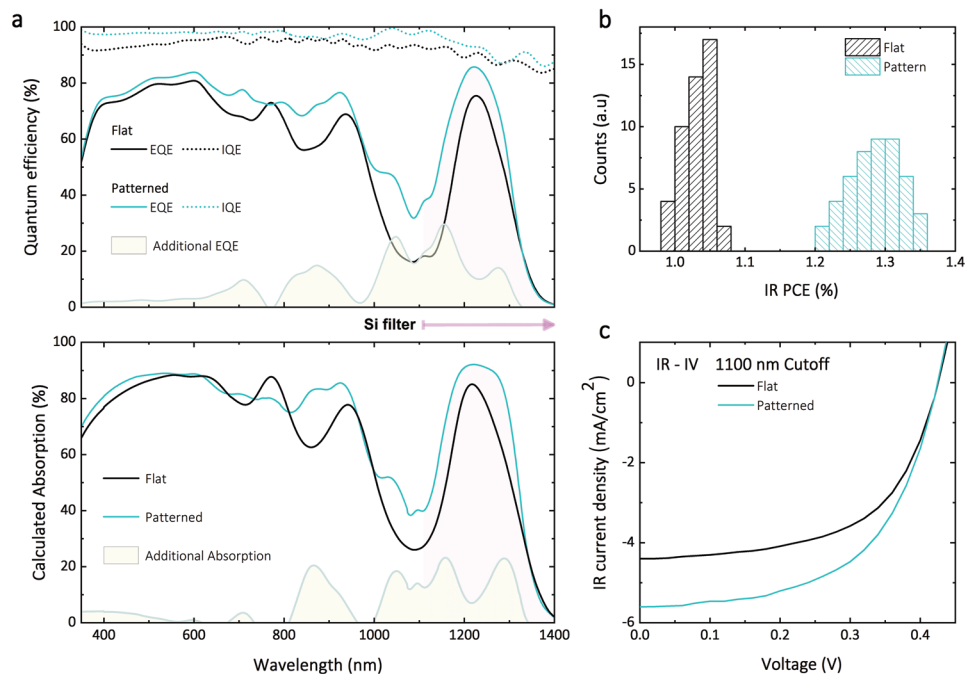


Figure 4. a) Experimental EQE and IQE (dots) (up) and calculated absorption (down) spectrum of IR CQD device with (blue) and without (black) imprinting. The grey area depicts the additional EQE/absorption enhanced with the photonic electrode. b) Statistical histogram of PCE of IR CQD devices with (blue) and without (black) imprinting. c) Representative J - V curves of IR CQD devices with (turquoise) and without (black) imprinting. The J - V was measured after the 1100 nm cutoff filter (purple region in (a)).

Table 1. IR CQD solar cells parameters characterized under AM 1.5G with 1100 nm cutoff filter.

1188 nm CQD	V_{oc} [V]	J_{sc} [mA cm^{-2}]	FF	IR PCE ^{a)} [%]	+ c-Si PCE ^{b)} [%]
Flat	0.43 ± 0.00^c (0.43) ^{d)}	4.3 ± 0.08 (4.4)	0.56 ± 0.10 (0.57)	5.25 ± 0.11 (5.51)	1.03 ± 0.02 (1.08)
Patterned	0.43 ± 0.00 (0.43)	5.4 ± 0.14 (5.6)	0.55 ± 0.15 (0.56)	6.50 ± 0.15 (6.83)	1.27 ± 0.03 (1.34)

^{a)}Calculated IR PCE under the filtered AM 1.5 solar spectrum (19.1 mW cm^{-2} , cutoff <1100 nm); ^{b)}Added IR PCE to c-Si solar cells under the AM 1.5 solar irradiation; ^{c)}Average solar cells parameters and standard deviations; ^{d)}Brackets depict the best values at each parameter.

Experimental Section

IR CQD Device Fabrication: The oleate-capped PbS CQDs and ZnO nanoparticles were synthesized following the previous reports.^[23] The mixture of PbI_2 (40 mmol)/ PbBr_2 (20 mmol)/ PbCl_2 (40 mmol) dissolved in dimethylformamide (DMF) solution was prepared in previous day. For ligand exchange, 1188 nm PbS CQD dissolved in octane (50 mg mL^{-1}) was injected to the mixture solution (octane:precursor solution = 1:1) followed by vigorous mixing for 5 min until the CQDs completely transferred to the DMF phase. The exchanged CQDs were washed by octane at least three times. The final CQDs were precipitated by adding the 1.5 mL of acetone at each 2.5 mL of CQD solution. After centrifugation, drying CQD dot at the vacuum oven for 10 min and redispersed into a mixture of butylamine:DMF (8:2) at the concentration of 280 mg mL^{-1} . The CQD solution was spun onto the prepared ITO/ZnO layers via a two-step spin-coating process under N_2 purging: 600 rpm for 10 s followed up by 1000 rpm for 20 s. The resultant films were dried at $70 \text{ }^\circ\text{C}$ for 5 min in the glove box. Films with the CQD layers were stored for one day in air before the deposition of subsequent layers. For CQD-EDT HTL, two layers of EDT-treated CQDs were deposited based on the previous report.^[24] For organic HTL, the prepared organic solution (15 mg mL^{-1}) was spun onto the CQD layer at 2500 rpm for 30 s followed by drying at $80 \text{ }^\circ\text{C}$ for 5 min. In particular, the spinning time was reduced from 30 to 7 s for imprinted device to form 2D photonic structure before the organic layer was fully dried. Finally, 20 nm of MoO_3 and 400 nm of Ag were deposited through the shadow mask. The entire active device area during the measurement was 4.9 cm^2 .

Nanoimprinting Procedure: Organic HTL 2D photonic crystals were fabricated by nanoimprint lithography using polydimethylsiloxane (soft-PDMS) molds with patterned areas of 1 cm^2 . These molds consist on an array of pillars with a diameter of 200 nm, 300 nm tall in a 500 nm square periodicity. The imprinting was done right after the spinning of the organic HTL (see previous IR CQD device fabrication section) while the film was still viscous, applying a pressure of 25 Pa. Regulating the applied pressure, the depth of the imprinted pattern was controlled. After pressing for 2 min, we slowly removed the PDMS mold and dried the sample at $80 \text{ }^\circ\text{C}$. It was found important to release the PDMS stamp at a slow rate to ensure a peel-off that did not disrupt the pattern. The peeling-off rate employed was kept below 1 mm s^{-1} .

SCLC Measurement: The entire structure of SCLC device was ITO (100 nm)/ MoO_3 (20 nm)/HTL (65 nm)/ MoO_3 (20 nm)/Ag (120 nm). Thickness of HTLs was adjusted by changing spinning speed. For mobility calculation, dielectric constant (ϵ) of polymer and PbS CQD were 4 and 25, respectively, based on the previous report.^[25]

Solar Cells Measurements: EQE and IQE spectra were acquired on a QuantX-300 quantum efficiency measurement system (Newport). Monochromatic white light from a xenon lamp was chopped at a frequency of 25 Hz. EQE spectra were acquired at zero electrical bias. IQE spectra were calculated using EQE spectra taken at -2 V (ensuring extraction of all photogenerated carriers) as $\text{IQE} = \text{EQE}(0 \text{ V}) / \text{EQE}(-2 \text{ V})$.^[26] Biased EQE is displayed in Figure S5 (Supporting Information). The estimated IQE agrees well that was seen in IR CQD

solar cells reported previously.^[27] The J - V under a simulated AM1.5 solar spectrum was acquired and corrected according to EQE spectra. Devices were kept in an inert N_2 atmosphere. The input power density was adjusted to 1 sun using a NIST-traceable calibrated reference cell (Newport 91 150 V). To account for the spectral mismatch between the AM1.5 G reference spectrum and the spectrum of the lamp, a current density correction factor was used for each device, corresponding to the ratio of the value calculated from integrating the EQE spectrum and the value measured under illumination. The lamp spectrum was measured using irradiance-calibrated spectrometers (USB2000 and NIR512, Ocean Optics).

Other Characterizations: Absorbance measurements were performed on a Lambda 950 UV-Vis-IR spectrometer. Hitachi S-5200 microscope was used to obtain SEM images. AFM study was performed with an Asylum Research Cypher AFM equipped with AC240TM-R3 probes.

Optical Modelling: The numerical calculations were performed using Lumerical FDTD solutions (www.lumerical.com). The refractive indexes of the CQD and organic layers were extracted from ellipsometry data. The simulated architecture reproduced the schematic shown in Figure 3d with the geometrical parameters extracted from SEM of the actual samples. A linearly polarized plane wave source impinging a unit cell was modeled with a wavelength ranging from 350 to 1400 nm, providing a good agreement with experimental results.

Supporting Information

Supporting Information is available from the Wiley Online Library or from the author.

Acknowledgements

S.-W.B., P.M., and M.-J.C. contributed equally to this work. This work was supported by Ontario Research Fund-Research Excellence program (ORF7-Ministry of Research and Innovation, Ontario Research Fund-Research Excellence Round 7), and by the Natural Sciences and Engineering Research Council (NSERC) of Canada. This work was also supported by the National Research Foundation of Korea (NRF) funded by NRF-2018R1A6A3A03012630. The authors thank the Spanish Ministry of Economy and Competitiveness (MINECO) for its support through grant nos. MAT2016-79053-P and SEV-2015-0496. This project received funding from the European Research Council (ERC) under the European Union's Horizon 2020 research and innovation programme (grant no. 637116). The authors thank L. Levina, R. Wolowiec, D. Kopilovic, E. Palmiano, and J. L. Garcia-Pomar for their help over the course of this research.

Conflict of Interest

The authors declare no conflict of interest.

Keywords

colloidal quantum dots, conjugated polymers, hole transporting layers, infrared optoelectronics, nanoimprinting

Received: March 19, 2019

Revised: May 10, 2019

Published online:

- [1] C. R. Kagan, E. Lifshitz, E. H. Sargent, D. V. Talapin, *Science* **2016**, 353, aac5523.
- [2] F. P. G. de Arquer, A. Armin, P. Meredith, E. H. Sargent, *Nat. Rev. Mater.* **2017**, 2, 16100.
- [3] S. W. Baek, J. Cho, J. S. Kim, C. Kim, K. Na, S. H. Lee, S. Jun, J. H. Song, S. Jeong, J. W. Choi, *Adv. Mater.* **2018**, 30, 1707224.
- [4] A. Karani, L. Yang, S. Bai, M. H. Futscher, H. J. Snaith, B. Ehrler, N. C. Greenham, D. Di, *ACS Energy Lett.* **2018**, 3, 869.
- [5] A. H. Ip, A. Kiani, I. J. Kramer, O. Voznyy, H. F. Movahed, L. Levina, M. M. Adachi, S. Hoogland, E. H. Sargent, *ACS Nano* **2015**, 9, 8833.
- [6] J. Kim, O. Ouellette, O. Voznyy, M. Wei, J. Choi, M. J. Choi, J. W. Jo, S. W. Baek, J. Fan, M. I. Saidaminov, *Adv. Mater.* **2018**, 30, 1803830.
- [7] a) S.-W. Baek, O. Ouellette, J. W. Jo, J. Choi, K.-W. Seo, J. Kim, B. Sun, S.-H. Lee, M.-J. Choi, D.-H. Nam, *ACS Energy Lett.* **2018**, 3, 2908; b) X. Zhang, E. M. Johansson, *Nano Energy* **2016**, 28, 71; c) O. Ouellette, N. Hossain, B. R. Sutherland, A. Kiani, F. P. García de Arquer, H. Tan, M. Chaker, S. Hoogland, E. H. Sargent, *ACS Energy Lett.* **2016**, 1, 852.
- [8] a) T. Kawawaki, H. Wang, T. Kubo, K. Saito, J. Nakazaki, H. Segawa, T. Tatsuma, *ACS Nano* **2015**, 9, 4165; b) S. W. Baek, J. H. Song, W. Choi, H. Song, S. Jeong, J. Y. Lee, *Adv. Mater.* **2015**, 27, 8102; c) S. W. Baek, G. Park, J. Noh, C. Cho, C. H. Lee, M. K. Seo, H. Song, J. Y. Lee, *ACS Nano* **2014**, 8, 3302; d) S. W. Baek, J. Noh, C. H. Lee, B. Kim, M. K. Seo, J. Y. Lee, *Sci. Rep.* **2013**, 3, 1726; e) S. Chen, Y. j. Wang, Q. Liu, G. Shi, Z. Liu, K. Lu, L. Han, X. Ling, H. Zhang, S. Cheng, *Adv. Energy Mater.* **2018**, 8, 1701194.
- [9] C. Matricardi, C. Hanske, J. L. Garcia-Pomar, J. Langer, A. Mihi, L. M. Liz-Marzán, *ACS Nano* **2018**, 12, 8531.
- [10] Y. Kim, K. Bicanic, H. Tan, O. Ouellette, B. R. Sutherland, F. P. García de Arquer, J. W. Jo, M. Liu, B. Sun, M. Liu, *Nano Lett.* **2017**, 17, 2349.
- [11] A. Mihi, F. J. Beck, T. Lasanta, A. K. Rath, G. Konstantatos, *Adv. Mater.* **2014**, 26, 443.
- [12] a) V. E. Ferry, A. Polman, H. A. Atwater, *ACS Nano* **2011**, 5, 10055; b) M. G. Deceglie, V. E. Ferry, A. P. Alivisatos, H. A. Atwater, *Nano Lett.* **2012**, 12, 2894.
- [13] a) X. H. Li, W. C. H. Choy, L. J. Huo, F. X. Xie, W. E. I. Sha, B. F. Ding, X. Guo, Y. F. Li, J. H. Hou, J. B. You, Y. Yang, *Adv. Mater.* **2012**, 24, 3046; b) S. Jeong, C. Cho, H. Kang, K. H. Kim, Y. Yuk, J. Y. Park, B. J. Kim, J. Y. Lee, *ACS Nano* **2015**, 9, 2773.
- [14] Y. Wang, P. Wang, X. Zhou, C. Li, H. Li, X. Hu, F. Li, X. Liu, M. Li, Y. Song, *Adv. Energy Mater.* **2018**, 8, 1702960.
- [15] M. M. Huo, R. Liang, Y. D. Xing, R. Hu, N. J. Zhao, W. Zhang, L. M. Fu, X. C. Ai, J. P. Zhang, J. H. Hou, *J. Chem. Phys.* **2013**, 139, 124904.
- [16] V. D. Mihailetschi, J. Wildeman, P. W. M. Blom, *Phys. Rev. Lett.* **2005**, 94, 126602.
- [17] a) K. Feng, X. Xu, Z. Li, Y. Li, K. Li, T. Yu, Q. Peng, *Chem. Commun.* **2015**, 51, 6290; b) R. Azmi, S. Sinaga, H. Aqoma, G. Seo, T. K. Ahn, M. Park, S.-Y. Ju, J.-W. Lee, T.-W. Kim, S.-H. Oh, *Nano Energy* **2017**, 39, 86.
- [18] P. Molet, J. L. Garcia-Pomar, C. Matricardi, M. Garriga, M. I. Alonso, A. Mihi, *Adv. Mater.* **2018**, 30, 1705876.
- [19] a) Y. Xia, G. M. Whitesides, *Angew. Chem., Int. Ed.* **1998**, 37, 550; b) Y. Xia, J. A. Rogers, K. E. Paul, G. M. Whitesides, *Chem. Rev.* **1999**, 99, 1823.
- [20] C. Dore, J. Osmond, A. Mihi, *Nanoscale* **2018**, 10, 17884.
- [21] Y. Bi, S. Pradhan, S. Gupta, M. Z. Akgul, A. Stavrinadis, G. Konstantatos, *Adv. Mater.* **2018**, 30, 1704928.
- [22] J. Choi, J. W. Jo, F. P. G. de Arquer, Y. B. Zhao, B. Sun, J. Kim, M. J. Choi, S. W. Baek, A. H. Proppe, A. Seifitokaldani, *Adv. Mater.* **2018**, 30, 1801720.
- [23] M. Liu, O. Voznyy, R. Sabatini, F. P. Garcia de Arquer, R. Munir, A. H. Balawi, X. Lan, F. Fan, G. Walters, A. R. Kirmani, S. Hoogland, F. Laquai, A. Amassian, E. H. Sargent, *Nat. Mater.* **2017**, 16, 258.
- [24] C. H. M. Chuang, P. R. Brown, V. Bulovic, M. G. Bawendi, *Nat. Mater.* **2014**, 13, 796.
- [25] a) D. D. Grinolds, P. R. Brown, D. K. Harris, V. Bulovic, M. G. Bawendi, *Nano Lett.* **2015**, 15, 21; b) Z. He, C. Zhong, X. Huang, W. Y. Wong, H. Wu, L. Chen, S. Su, Y. Cao, *Adv. Mater.* **2011**, 23, 4636.
- [26] Q. Lin, A. Armin, R. C. R. Nagiri, P. L. Burn, P. Meredith, *Nat. Photonics* **2015**, 9, 106.
- [27] B. Sun, O. Ouellette, F. P. García de Arquer, O. Voznyy, Y. Kim, M. Wei, A. H. Proppe, M. I. Saidaminov, J. Xu, M. Liu, P. Li, J. Z. Fan, J. W. Jo, H. Tan, F. Tan, S. Hoogland, Z. H. Lu, S. O. Kelley, E. H. Sargent, *Nat. Commun.* **2018**, 9, 4003.